Optimizing thermal management in battery electric vehicle powertrains with energy-efficient model predictive control

Citation for the original published paper (version of record):

Xu, Y., Klacar, S., George, S. et al (2026). Optimizing thermal management in battery electric vehicle powertrains with energy-efficient model predictive control. Applied Thermal Engineering, 289. http://dx.doi.org/10.1016/j.applthermaleng.2026.129897

Applied Thermal Engineering 289 (2026) 129897

Contents lists available at ScienceDirect

Applied Thermal Engineering

journal homepage: www.elsevier.com/locate/ate

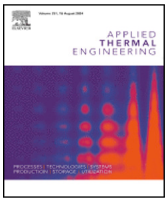

Research Paper

Optimizing thermal management in battery electric vehicle powertrains with energy-efficient model predictive control

Y. Xu [a,b,*], S. Klacar [c], S. George [c], A. Andersson [c], D. Sedarsky [b], A. Kersten [d]

[a] *Zeekr Technology Europe AB, Göteborg, Sweden*
[b] *Chalmers University of Technology, Division of Transport, Energy and Environment, Mechanics and Maritime Sciences, Göteborg, Sweden*
[c] *Infimotion Technology Europe AB, Göteborg, Sweden*
[d] *Technical University of Applied Sciences Lübeck, Science Center for Electromobility, Power Electronics and Decentralized Energy Supply, Lübeck, Germany*

ARTICLE INFO

Keywords:
Battery electric vehicle (BEV)
Energy efficiency
Powertrain
Model predictive control (MPC)
Thermal aging

ABSTRACT

Thermal management is critical for energy efficiency and reliability in battery electric vehicle (BEV) powertrains. Conventional rule-based strategies often prioritize thermal safety over efficiency. This study presents a model predictive control (MPC)-based thermal management strategy for a BEV powertrain with a mixed coolant/oil cooling architecture. The MPC framework utilizes a control-oriented model to minimize battery energy consumption while adhering to thermal constraints for the inverter, electric motor, and transmission. Simulations over representative real-world driving cycles show that the MPC-based strategy reduces battery energy consumption by 0.26% in urban driving and 1.06% in highway driving compared to a rule-based benchmark. The thermal durability of the inverter and motor is evaluated, showing that the impact of the MPC-based strategy varies with the driving profile: lifetimes improve under urban driving due to enhanced cooling, but degrade under sustained highway operation as higher temperatures are allowed. For a representative daily round-trip commute, the estimated lifetimes of the inverter ($10,100$ h) and motor ($20,100$ h) nevertheless exceed typical BEV durability requirements. These findings demonstrate that MPC-based thermal management can achieve significant energy savings without compromising component longevity.

1. Introduction

Escalating concerns regarding environmental sustainability and the need to reduce reliance on fossil fuels have spurred a global shift towards battery electric vehicles (BEVs) in the automotive sector [1,2]. Although BEV market penetration continues to rise, several challenges persist. Notably limited driving range and inadequate charging infrastructure, which contribute to range anxiety among consumers [3–5]. Enhancing the energy efficiency of BEVs is crucial for addressing these concerns and accelerating the widespread adoption of these vehicles.

One key factor affecting the energy efficiency of a BEV powertrain is operating temperature [6,7]. Specifically, the temperature-dependent efficiency of the main powertrain components — the inverter, electric motor, and transmission — has been extensively studied. In the electric motor, temperature variations affect both copper and iron losses [8–10]. Similarly, the conduction and switching losses in the inverter are influenced by the temperature of its semiconductor devices [11–13]. Additionally, the transmission is temperature-sensitive owing to the temperature-dependent viscosity of the lubricating oil, affecting churning and frictional losses [14,15]. However, conventional thermal management strategies for electric powertrains typically rely on rule-based controls, where cooling system components, such as pumps and fans, operate proportionally to maintain temperatures within safe limits and prevent overheating [16,17]. These approaches often result in overly conservative operation, leading to unnecessary energy consumption in both powertrain components and the cooling system.

Various studies focus on energy-oriented thermal management of electric powertrains by leveraging the temperature-dependent efficiency characteristics of key powertrain components, as summarized in Table 1. For example, torque split strategies proposed in [18,19] enhance energy efficiency by considering temperature-dependent motor efficiency. Similarly, [20] optimizes torque distribution based on the temperature-dependent efficiency of the inverter. These works establish a connection between component thermal behavior and powertrain energy management; however, they largely neglect the influence of the cooling system and its thermal management strategy.

---

[*] Corresponding author at: Chalmers University of Technology, Division of Transport, Energy and Environment, Mechanics and Maritime Sciences, Göteborg, Sweden.

E-mail address: yuxu@chalmers.se (Y. Xu).

https://doi.org/10.1016/j.applthermaleng.2026.129897
Received 20 October 2025; Received in revised form 9 January 2026; Accepted 21 January 2026

Nomenclature

Abbreviations

AGS	Active grill shutter
BEV	Battery electric vehicle
IPMSM	Interior permanent magnet synchronous motor
LPTN	Lumped parameter thermal network
MPC	Model predictive control
OCP	Optimal control problem
RMSE	Root mean square error
WLTC	Worldwide harmonized light vehicles test cycle

Symbols

$\dot{m}$	Mass flow rate [kg s^{-1}]
$\dot{V}$	Volumetric flow rate [L min^{-1}]
ϕ	Active grill shutter position angle [°]
ρ	Density [kg m^{-3}]
θ	Road slope angle [°]
A	Area [m^{2}]
C	Thermal capacitance [J K^{-1}]
C_d	Aerodynamic drag coefficient [-]
c_p	Specific heat capacity [J kg^{-1} K^{-1}]
C_r	Tire rolling resistance coefficient [-]
D	Damage [-]
d	Duty cycle[-]
E_{sw}	Switching energy [J]
F	Force [N]
f_{sw}	Switching frequency [Hz]
g	Gravitational acceleration [m s^{-2}]
h	Heat transfer coefficient [W m^{-2} K^{-1}]
I_p	Phase current [A]
LF	Lifetime [s] or [h]
LLF	Lifetime loss fraction [-]
M	Torque [N m]
m	Mass [kg]
N	Number of cycle [-]
n	Rotational speed [rpm]
N_p	Prediction and control horizon [-]
N_f	Number of cycle to failure [-]
P	Power [W]
p	Pressure [bar]
Q	Heat transfer rate [W]
R	Thermal resistance [K W^{-1}]
r_{ds}	Transistor on-state resistance [Ω]
T	Temperature [°Celsius]
t	Time [s]
U	Voltage [V]
u	Control input vector [-]
v	Speed [m s^{-1}]
x	State vector [-]

Subscripts

a	Ambient
c	Coolant
emci	Electric motor coolant inlet
emco	Electric motor coolant outlet
emc	Electric motor coolant
emoi	Electric motor oil inlet
emoo	Electric motor oil outlet
emo	Electric motor oil
em	Electric motor
ici	Inverter coolant inlet
ico	Inverter coolant outlet
ic	Inverter coolant
inv	Inverter
jt	Junction
ls	Loss
occo	Oil cooler coolant outlet
oc	Oil cooler
o	Oil
pm	Permanent magnet
pu	Pump
rad	Radiator
ref	Reference
so	Sump oil
trac	Traction
tran	Transmission
veh	Vehicle
w	Winding

Other studies focus primarily on reducing the energy consumption of cooling auxiliaries such as pumps and fans. In [21], a nonlinear tracking controller regulates cooling system operation, achieving a 68% reduction in cooling power consumption over an urban drive cycle while maintaining the motor hot-spot temperature within limits. A fuzzy control-based strategy in [22] reduces pump and fan energy consumption by up to 28% in an inverter–motor cooling loop. Likewise, [23] introduces an MPC-based thermal management approach using a lumped-parameter thermal network (LPTN) model, reducing fan power by 73% with only a 5% increase in pump power over a 60-min driving cycle. However, these studies focus exclusively on minimizing cooling-system energy and do not consider the temperature-dependent efficiency characteristics of the powertrain components themselves.

Recent research has adopted a holistic approach to manage component temperatures, minimizing overall energy consumption of the powertrain and cooling system while respecting thermal constraints. For instance, [24] formulates an optimal control problem (OCP) to minimize motor losses and pump energy use, achieving a 12% reduction in battery energy consumption. Similarly, [25] proposes a strategy that simultaneously minimizes cooling-system power (blower and pump) and motor losses, resulting in an 86% reduction in combined energy losses during an urban drive cycle. Despite the strong thermal coupling among components and their differing optimal operating temperatures, many studies still target individual components or subsystems. In contrast, [26,27] introduce an MPC-based thermal management framework that jointly optimizes energy usage of the cooling system, inverter, and motor to minimize total vehicle energy consumption. This concept is further expanded in [28], which incorporates both coolant and oil circuits within a more complex cooling architecture, demonstrating the potential of MPC for advanced integrated powertrain systems.

Most existing studies have not addressed the temperature-dependent efficiency characteristics of transmission, especially with the recent emergence of integrated electric drive units, where the inverter, electric motor, and transmission are packaged together [29–31]. This integration often necessitates advanced thermal management systems owing to increased thermal interactions among components and the presence of both coolant and oil circuits, as the transmission typically shares the same oil circuit with the motor to enhance cooling performance and power density [32,33]. This close coupling necessitates

Table 1
Previous studies on energy-oriented powertrain thermal management strategies.

Minimization objective	References
Powertrain energy consumption	[18–20]
Cooling system energy consumption	[21–23]
Powertrain & cooling energy consumption	[24–28], This study

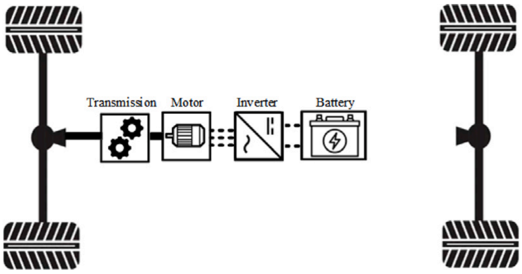

Fig. 1. Powertrain configuration.

incorporating the transmission into the thermal management framework, as it necessitates active cooling beyond conventional passive methods and presents an additional opportunity for optimizing overall energy efficiency through coordinated, system-level thermal management. Additionally, prior studies indicate that optimization-based thermal management strategies may enhance powertrain energy efficiency by operating components at higher temperatures [26,27]. However, the long-term durability implications of sustained high-temperature operation on critical components, particularly the inverter and motor, remain unclear [25,34,35]. Because temperature significantly influences component aging and lifetime, further investigation is essential to assess potential long-term degradation.

To address this gap, this study proposes an MPC-based thermal management strategy that utilizes a comprehensive control-oriented thermal model, accounting for the inverter, motor, and transmission. The optimization problem aims to minimize overall energy consumption, including powertrain component losses and auxiliary power demands from the powertrain cooling system. Additionally, the impact of elevated operating temperatures on the lifetime of critical components is evaluated. The remainder of this study is organized as follows: Section 2 describes the examined powertrain architecture and cooling system layout. Section 3 presents the development of the control-oriented model used in the MPC framework. Section 4 identifies unknown parameters in the control-oriented model through curve fitting and system identification techniques. Section 5 outlines the baseline rule-based thermal management strategy and formulates the proposed MPC-based control problem. Section 6, discusses the simulation setup and energy efficiency improvements, whereas Section 7 evaluates the impact of thermal management strategies on powertrain component lifetime. Finally, Section 8 summarizes the conclusions.

2. System setup

The powertrain investigated in this study is a single-motor configuration (see Fig. 1), comprising a coolant-cooled inverter with SiC MOSFET modules, a coolant-oil mixed-cooled interior permanent magnet synchronous machine (IPMSM), and a single-speed transmission with oil splash. The powertrain operates with a 400 V battery DC voltage supply and delivers a peak power output of 120 kW.

Fig. 2 illustrates the schematic of the investigated powertrain cooling system, comprising interconnected coolant and oil circuits. In the oil circuit, an electric oil pump circulates oil from the sump through the oil cooler. The cooled oil is delivered to spray channels, where it is injected onto the motor end windings via spray nozzles and flows into the transmission for lubrication and cooling. Finally, the oil returns to the sump by gravity.

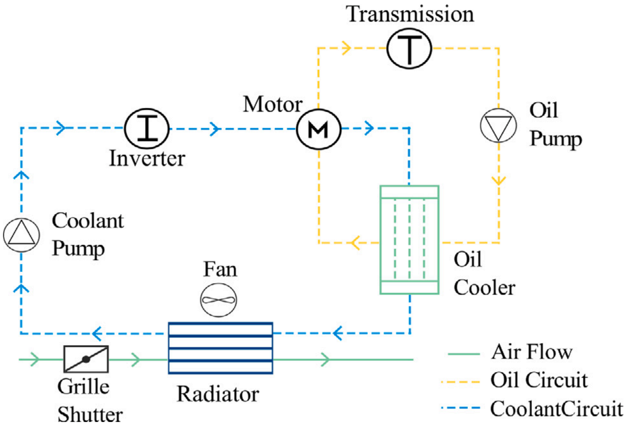

Fig. 2. Schematic of the investigated powertrain cooling system.

In the coolant circuit, an electric coolant pump circulates a water-glycol mixture (EGL5050) through the inverter cooling channel, the motor housing water jacket, and the oil cooler. After absorbing heat from these components, the heated coolant flows into the radiator, where it dissipates thermal energy into the ambient air. Airflow through the radiator is controlled by a radiator fan and an actively regulated shutter grille, which optimizes both cooling performance and aerodynamic efficiency.

3. Control-oriented model

In this section, a control-oriented model is developed to capture the thermal behavior of the powertrain components and cooling system. The inverter and motor are modeled using LPTNs, which represent heat transfer through equivalent electrical circuits [36,37]. The model is designed to be computationally efficient while preserving key dynamic characteristics required for the MPC framework described later. For compactness, a function of multiple variables is denoted as $(\cdot)$. Model fitting parameters to be identified or fitted are represented by α and β.

3.1. Vehicle dynamics

The total resistive force on a moving vehicle includes gradient resistance, aerodynamic drag, rolling resistance from the tires, and inertial resistance due to acceleration. These forces collectively determine the required wheel traction force:

$$F_{\mathrm{trac}} = \overbrace{mg\sin(\theta)}^{\text{Gradient res.}} + \overbrace{\frac{1}{2}\rho_{\mathrm{a}} C_d(\phi) A_{\mathrm{veh}} v^2}^{\text{Aerodyn. drag}} + \overbrace{C_r mg\cos(\theta)}^{\text{Rolling res.}} + \overbrace{m\dot{v}_{\mathrm{veh}}}^{\text{Acc. force}} \tag{1}$$

The aerodynamic drag coefficient is determined by active grille shutter (AGS) angle, an interpolation polynomial is chosen to fit measurement data as:

$$C_d(\phi) = \sum_{i=0}^{1} \alpha_{1,i}\, \phi^i \tag{2}$$

3.2. Thermal dynamics

3.2.1. Inverter thermal model

The inverter is cooled via a dedicated coolant channel with a pin-fin heat sink [38]. Fig. 3 illustrates the inverter geometry and the reduced-order LPTN, focusing on junction and coolant outlet temperatures.

For simplicity, the inverter loss power $P_{\mathrm{ls,inv}}$ is assigned to the junction node, which represents the average temperature of the MOSFETs.

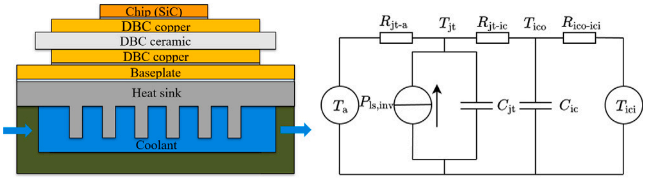

(a) (b)

Fig. 3. Inverter cooling system and thermal model: (a) 3D geometry and (b) reduced-order LPTN representation.

The generated heat is transferred by the thermal convection with the coolant, in addition to the thermal convection with the surrounding air in the powertrain compartment (assumed to be the same as ambient condition). The rate of change in the junction temperature T_{jt} and inverter coolant outlet temperature T_{ico} are expressed as:

$$\frac{dT_{\text{jt}}}{dt} = \frac{1}{C_{\text{jt}}}\left(P_{\text{ls,inv}} - \frac{T_{\text{jt}} - T_{\text{ico}}}{R_{\text{jt-c}}} - \frac{T_{\text{jt}} - T_{\text{a}}}{R_{\text{jt-a}}}\right) \tag{3}$$

$$\frac{dT_{\text{ico}}}{dt} = \frac{1}{C_{\text{ic}}}\left(\frac{T_{\text{jt}} - T_{\text{ico}}}{R_{\text{jt-ic}}} - \frac{T_{\text{ico}} - T_{\text{ici}}}{R_{\text{ico-ici}}}\right) \tag{4}$$

The thermal resistances associated with convective heat transfer to the coolant - $R_{\text{jt-c}}$ and $R_{\text{ico-ici}}$ - are modeled using the simplified approximation proposed by Semikron [39], which accounts for their dependence on the coolant flow rate $\dot{V}_{\text{c}}$ as:

$$R = R_{\text{ref}}\left(\frac{\dot{V}_{\text{c}}}{\dot{V}_{\text{ref}}}\right)^{\beta} \tag{5}$$

Owing to the high level of abstraction in the LPTN model, the thermal resistances $R_{\text{jt-a}}$, $R_{\text{jt-c,ref}}$, and $R_{\text{ico-ici,ref}}$, the thermal capacitances C_{jt} and C_{ico}, as well as the coefficients β, are subject to parameter identification.

3.2.2. *Motor thermal model*

A low-order LPTN estimates the temperatures of critical components within the motor, similar to the inverter. The motor employs a combined coolant and oil cooling strategy, where coolant circulates through a housing water jacket, and oil is sprayed directly onto the end windings to enhance thermal performance, as illustrated in Fig. 4(a). Natural convection between the motor surface and surrounding air is also considered, as it is with the inverter.

The adopted motor LPTN model, shown in Fig. 4, estimates the temperatures of the winding T_{w}, permanent magnet T_{pm}, motor coolant outlet T_{emco} and motor oil outlet T_{emoo}. For simplicity, the power loss within the stator and winding is aggregated as a single heat source $P_{\text{ls,w}}$, at the winding node. Similarly, losses in the permanent magnet and rotor are combined into a single heat source $P_{\text{ls,pm}}$, at the magnet node. The rate of change in the temperatures are expressed as:

$$\frac{dT_{\text{w}}}{dt} = \frac{1}{C_{\text{w}}}\left(P_{\text{ls,w}} - \frac{T_{\text{w}} - T_{\text{emco}}}{R_{\text{emco-w}}} - \frac{T_{\text{w}} - T_{\text{pm}}}{R_{\text{w-pm}}} - \frac{T_{\text{w}} - T_{\text{emoo}}}{R_{\text{emoo-w}}}\right) \tag{6}$$

$$\frac{dT_{\text{pm}}}{dt} = \frac{1}{C_{\text{pm}}}\left(P_{\text{ls,pm}} + \frac{T_{\text{w}} - T_{\text{pm}}}{R_{\text{w-pm}}} + \frac{T_{\text{a}} - T_{\text{pm}}}{R_{\text{a-pm}}}\right) \tag{7}$$

$$\frac{dT_{\text{emco}}}{dt} = \frac{1}{C_{\text{emc}}}\left(\frac{T_{\text{w}} - T_{\text{emco}}}{R_{\text{emco-w}}} - \frac{T_{\text{emco}} - T_{\text{emci}}}{R_{\text{emco-emci}}}\right) \tag{8}$$

$$\frac{dT_{\text{emoo}}}{dt} = \frac{1}{C_{\text{emo}}}\left(\frac{T_{\text{w}} - T_{\text{emoo}}}{R_{\text{emoo-w}}} - \frac{T_{\text{emoo}} - T_{\text{emoi}}}{R_{\text{emoo-emoi}}} + \frac{T_{\text{a}} - T_{\text{emoo}}}{R_{\text{a-emoo}}}\right) \tag{9}$$

Similar to the inverter, the thermal resistances associated with convective heat transfer to the coolant and oil – $R_{\text{emoo-w}}$, $R_{\text{emco-w}}$, $R_{\text{emco-emci}}$, and $R_{\text{emoo-emoi}}$ – are modeled as in (5).

The thermal resistances $R_{\text{emco-w,ref}}$, $R_{\text{emco-emci,ref}}$, $R_{\text{emoo-w,ref}}$, $R_{\text{emoo-emoi,ref}}$, $R_{\text{a-emoo}}$, $R_{\text{w-pm}}$, and $R_{\text{a-pm}}$, the thermal capacitances C_{emc}, C_{emo}, C_{w}, and C_{pm}, as well as the coefficients β, are subject to parameter identification.

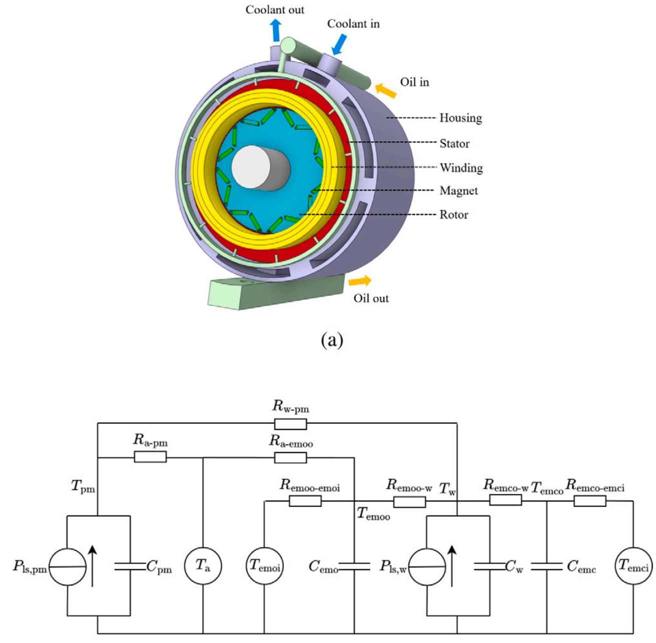

(a)

(b)

Fig. 4. Motor cooling system and thermal model: (a) 3D geometry and (b) reduced-order LPTN representation.

3.2.3. *Transmission thermal model*

Heat transfer within the transmission occurs through natural convection with surrounding air in the powertrain compartment and convection to the lubricating oil, both from dripping oil exiting the motor and the immersion of gear pairs in the oil sump. The simplified thermal model emphasizes the oil sump temperature T_{so}, as it correlates strongly with the transmission's power losses [40,41]. The sump oil exchanges heat directly with ambient air using an effective heat transfer coefficient h_{so} and area A_{so}. The transmission power losses from gear mesh and bearing friction are introduced as heat sources into the oil mass and are assumed to be uniformly distributed. Applying the first law of thermodynamics to the oil control volume yields the general energy balance:

$$m_{\text{so}}c_{p,\text{o}}\frac{dT_{\text{so}}}{dt} = \dot{m}_{\text{emoo}}c_{p,\text{o}}(T_{\text{emoo}} - T_{\text{so}}) + P_{\text{ls,tran}} - h_{\text{so}}A_{\text{so}}(T_{\text{so}} - T_{\text{a}}) \tag{10}$$

The product of the effective heat transfer coefficient and area, $h_{\text{so}}A_{\text{so}}$, is subject to parameter identification.

3.2.4. *Pump*

A static component model represents both the coolant and oil pumps. The electrical power consumption of each pump is estimated using a polynomial fit of the measurement data, based on fluid flow rate and corresponding pressure rise:

$$P_{\text{pu,c}}(\dot{V}_{\text{c}}, \Delta p_{\text{pu,c}}) = \sum_{i=0}^{3}\sum_{j=0}^{1}\alpha_{2,ij}\dot{V}_{\text{c}}^{i}\Delta p_{\text{pu,c}}^{j}(\cdot) \tag{11}$$

$$P_{\text{pu,o}}(\dot{V}_{\text{o}}, \Delta p_{\text{pu,o}}) = \sum_{i=0}^{3}\sum_{j=0}^{1}\alpha_{3,ij}\dot{V}_{\text{o}}^{i}\Delta p_{\text{pu,o}}^{j}(\cdot) \tag{12}$$

The pressure drops in the coolant circuit — across the radiator ($\Delta p_{\text{rad,c}}$), inverter cooling channel ($\Delta p_{\text{inv,c}}$), motor housing water jacket ($\Delta p_{\text{em,c}}$) and oil cooler ($\Delta p_{\text{oc,c}}$) — as well as those in the oil circuit — across the oil cooler ($\Delta p_{\text{oc,o}}$) and motor oil spray channel ($\Delta p_{\text{em,o}}$) — are modeled using polynomial fits based on measurement data. Each pressure drop is expressed as a function of fluid flow rate and inlet temperature. For simplicity, pressure losses in connecting pipes are neglected. Thus, the required pressure rise of the coolant pump $\Delta p_{\mathrm{pu,c}}$ and oil pump $\Delta p_{\mathrm{pu,o}}$ are approximated as the sum of the major component pressure drops:

$$\begin{aligned}\Delta p_{\mathrm{pu,c}}(\cdot) &= \Delta p_{\mathrm{rad,c}}(\dot{V}_{\mathrm{c}}, T_{\mathrm{occo}}) + \Delta p_{\mathrm{inv,c}}(\dot{V}_{\mathrm{c}}, T_{\mathrm{ici}}) \\ &\quad + \Delta p_{\mathrm{em,c}}(\dot{V}_{\mathrm{c}}, T_{\mathrm{emci}}) + \Delta p_{\mathrm{oc,c}}(\dot{V}_{\mathrm{c}}, T_{\mathrm{emco}}) \\ &= \sum_{i=0}^{2}\sum_{j=0}^{1}\big(\alpha_{4,ij}\dot{V}_{\mathrm{c}}^{i}T_{\mathrm{occo}}^{j} + \alpha_{5,ij}\dot{V}_{\mathrm{c}}^{i}T_{\mathrm{ici}}^{j} \\ &\quad + \alpha_{6,ij}\dot{V}_{\mathrm{c}}^{i}T_{\mathrm{emci}}^{j} + \alpha_{7,ij}\dot{V}_{\mathrm{c}}^{i}T_{\mathrm{emco}}^{j}\big)\end{aligned} \tag{13}$$

$$\begin{aligned}\Delta p_{\mathrm{pu,o}}(\cdot) &= \Delta p_{\mathrm{oc,o}}(\dot{V}_{\mathrm{o}}, T_{\mathrm{so}}) + \Delta p_{\mathrm{em,o}}(\dot{V}_{\mathrm{o}}, T_{\mathrm{emoi}}) \\ &= \sum_{i=0}^{2}\sum_{j=0}^{1}\big(\alpha_{8,ij}\dot{V}_{\mathrm{o}}^{i}T_{\mathrm{so}}^{j} + \alpha_{9,ij}\dot{V}_{\mathrm{o}}^{i}T_{\mathrm{emoi}}^{j}\big)\end{aligned} \tag{14}$$

3.2.5. *Heat exchanger*

The coolant temperature at the radiator inlet is assumed equal to the oil cooler outlet temperature T_{occo}. The radiator outlet temperature is taken as the inverter coolant inlet temperature T_{ici}. The oil cooler coolant inlet temperature is set to the motor coolant outlet temperature T_{emco}. On the oil side, the cooler inlet temperature is assumed equal to the sump oil temperature T_{so}, and the outlet temperature is assumed to be equal to the motor oil inlet temperature T_{emoi}.

For both the radiator and oil cooler, the heat transfer rate, Q, is modeled as a polynomial function of the fluid inlet temperatures and flow rates, fitted to measurement data. The radiator heat transfer rate Q_{rad} is fitted as a function of the coolant flow rate $\dot{V}_{\mathrm{c}}$, air mass flow rate $\dot{m}_{\mathrm{a}}$, and radiator coolant inlet temperature T_{occo} for a specific ambient temperature:

$$Q_{\mathrm{rad}} = \sum_{i=0}^{2}\sum_{j=0}^{3}\sum_{k=0}^{1}\alpha_{10,ijk}\dot{V}_{c}^{\,i}\dot{m}_{\mathrm{a}}^{j}T_{\mathrm{occo}}^{k} \tag{15}$$

Similarly, the oil cooler heat transfer rate Q_{oc} is modeled as a function of the coolant flow rate $\dot{V}_{\mathrm{c}}$, oil flow rate $\dot{V}_{\mathrm{o}}$, oil cooler coolant inlet temperature T_{emco}, and oil inlet temperature T_{so}:

$$Q_{\mathrm{oc}} = \sum_{i=0}^{3}\sum_{j=0}^{2}\sum_{k=0}^{1}\sum_{l=0}^{1}\alpha_{11,ijk}\dot{V}_{c}^{\,i}\dot{V}_{o}^{\,j}T_{\mathrm{emco}}^{k}T_{\mathrm{so}}^{k} \tag{16}$$

Additionally, the air mass flow rate into the radiator is determined and approximated by the AGS position angle ϕ, fan PWM duty cycle d_{fan} and vehicle speed υ_{veh} using a polynomial fit of the measurement data:

$$\dot{m}_{\mathrm{air}} = \sum_{i=0}^{1}\sum_{j=0}^{2}\alpha_{12,ij}d_{\mathrm{fan}}^{i}\upsilon_{\mathrm{veh}}^{j}\cdot\sum_{k=0}^{2}\alpha_{13,k}\phi^{k} \tag{17}$$

3.2.6. *Fan*

As the ambient temperature T_{a} can be considered constant under a single driving case, the electrical power consumption of the fan is simplified as a polynomial function of the air mass flow rate and PWM duty cycle, based on measurement data:

$$P_{\mathrm{fan}}(\dot{m}_{\mathrm{air}}, d_{\mathrm{fan}}) = \sum_{i=0}^{1}\sum_{j=0}^{1}\alpha_{14,ij}\dot{m}_{\mathrm{air}}^{i}d_{\mathrm{fan}}^{j} \tag{18}$$

3.3. *Temperature-dependent powertrain loss*

3.3.1. *Inverter loss*

In the presented study, two SiC MOSFET CAS300M12BM2 half-bridge modules are connected in parallel for each phase leg, ensuring a peak current of 425 A is supplied to the motor. For the presented case, the voltage drop across the on-state resistance of the transistor, r_{ds}, is smaller than the forward voltage drop of the body diode. Therefore, it can be assumed that the body diodes of the MOSFETs do not conduct reverse current during the reverse conduction period; hence, conduction losses occur only in the transistors [42]. The inverter power loss can then be obtained with the following equation [43]:

$$P_{\mathrm{ls,inv}} = \frac{3}{2}I_{p}^{2}r_{ds} + 6f_{sw}E_{sw}\left(\frac{I_{p}}{\pi I_{\mathrm{ref}}}\right)\left(\frac{U_{\mathrm{DC}}}{U_{\mathrm{ref}}}\right)^{1.4} \tag{19}$$

For the current amplitude I_{p}, the current vector in an IPMSM is primarily determined by torque demand and motor speed. However, both magnet and winding temperatures significantly affect the required current magnitude [44,45]. To account for these dependencies, a detailed motor model in Motor-CAD is used to accurately map the current vector as a function of motor speed n_{em}, torque M_{em}, winding temperature T_{w}, and magnet temperature T_{pm}. For use in a control-oriented model, the resulting current amplitude I_{p} is approximated using a polynomial fit as:

$$I_{p}(\cdot) = \sum_{i=0}^{2}\sum_{j=0}^{2}\sum_{k=0}^{1}\sum_{l=0}^{1}\alpha_{15,ijkl}n_{\mathrm{em}}^{i}M_{\mathrm{em}}^{j}T_{\mathrm{w}}^{k}T_{\mathrm{pm}}^{l} \tag{20}$$

Apart from the temperature-dependent current usage, the on-state resistance and switching energy of the MOSFETs are estimated by a polynomial fit considering their dependency on the junction temperature T_{jt}:

$$r_{ds}(T_{\mathrm{jt}}) = \sum_{i=0}^{2}\alpha_{16,ij}T_{\mathrm{jt}}^{i} \tag{21}$$

$$E_{sw}(T_{\mathrm{jt}}) = \sum_{i=0}^{2}\alpha_{17,ij}T_{\mathrm{jt}}^{i} \tag{22}$$

3.3.2. *Motor loss*

The power loss $P_{\mathrm{ls,w}}$ in the winding node includes both copper and stator iron losses, whereas $P_{\mathrm{ls,pm}}$ includes magnet and rotor iron losses. These losses share the same dependency structure as the current amplitude and are approximated using polynomial fits to loss data derived from Motor-CAD simulation:

$$P_{\mathrm{ls,w}}(\cdot) = \sum_{i=0}^{2}\sum_{j=0}^{3}\sum_{k=0}^{1}\sum_{l=0}^{1}\alpha_{18,ijkl}n_{\mathrm{em}}^{i}M_{\mathrm{em}}^{j}T_{\mathrm{w}}^{k}T_{\mathrm{pm}}^{l} \tag{23}$$

$$P_{\mathrm{ls,pm}}(\cdot) = \sum_{i=0}^{3}\sum_{j=0}^{2}\sum_{k=0}^{1}\sum_{l=0}^{1}\alpha_{19,ijkl}n_{\mathrm{em}}^{i}M_{\mathrm{em}}^{j}T_{\mathrm{w}}^{k}T_{\mathrm{pm}}^{l} \tag{24}$$

3.3.3. *Transmission loss*

The transmission loss $P_{\mathrm{ls,tran}}$ is approximated as a function of motor speed n_{em}, motor torque M_{em}, and sump oil temperature T_{so}. A polynomial fit to measurement data is used to capture these dependencies:

$$P_{\mathrm{ls,tran}} = \sum_{i=0}^{1}\sum_{j=0}^{3}\sum_{k=0}^{2}\alpha_{20,ijk}n_{\mathrm{em}}^{i}M_{\mathrm{em}}^{j}T_{\mathrm{so}}^{k} \tag{25}$$

4. Model fitting and identification

This section outlines the fittings of component mappings and the identification of system parameters for the control-oriented model introduced in Section 3. The fitting and identification process is formulated as a standard least-squares optimization problem. Parameters are estimated to ensure that the outputs of the control-oriented model closely match the corresponding outputs from measurements, manufacturer data, or high-fidelity simulations.

The parameters characterizing the AGS, pumps, heat exchangers, fan, and temperature-dependent losses of powertrain components are fitted to static maps derived from measurements or data provided by manufacturers. The resulting fitted models show good agreement with the reference data across the considered operating range, achieving $R^2 > 0.98$. Specifically, Appendix A presents the residual errors between the fitted models and the original maps, shown as contour plots of the fitting error with respect to phase current, alongside the motor and transmission loss maps.

For parameters requiring identification owing to model abstraction — particularly for the inverter, motor, and transmission — the thermal dynamics described by Eqs. (3)–(10) are discretized using a forward Euler method with a 1 s sampling time. The inverter and transmission thermal parameters are identified against detailed 1D thermal models developed in GT-SUITE, whereas motor thermal parameters are identified using a high-order LPTN model generated in Motor-CAD, focusing on average winding and magnet temperatures.

To ensure robustness across various operating conditions, two standard legislative drive cycles validate the accuracy of the proposed control-oriented model: the Worldwide Harmonized Light Vehicles Test Cycle (WLTC) and the aggressive US06 drive cycle. The control-oriented model is validated against the high-fidelity 1D thermal model developed in GT-SUITE, which serves as the plant model in this study. The root mean square error (RMSE) of key powertrain node temperatures under different coolant and oil flow conditions is summarized in Table B.4. For the WLTC cycle, all temperature nodes exhibit RMSE values below approximately 2 °C, with typical errors well below 1 °C under nominal flow conditions. For the more aggressive US06 cycle, the RMSE remains consistently low, generally below 3 °C, even under reduced coolant and oil flow rates. Figs. B.15 and B.16 present detailed time-domain comparisons between the control-oriented model and the high-fidelity GT-SUITE reference model for key powertrain node temperatures under a representative coolant and oil flow condition, including the inverter junction temperature T_{jt}, motor winding temperature T_{w}, motor magnet temperature T_{pm}, and transmission sump oil temperature T_{so}, for both the WLTC and US06 driving conditions. The strong agreement observed over the wide operating range confirms that the proposed control-oriented model provides a high-fidelity yet computationally efficient representation of the full powertrain thermal dynamics.

5. Powertrain thermal management

The goal of powertrain thermal management is to maintain component temperatures within operational limits while ensuring efficient operation in optimal ranges. Conventionally, rule-based strategies assign temperature targets to each component, regulating auxiliary actuators (e.g., pumps and fans) to meet these targets. However, these approaches can result in overly conservative control and excessive energy consumption by auxiliaries.

This section introduces a rule-based thermal management strategy as the baseline. Subsequently, an energy-efficient thermal management strategy based on MPC is proposed. This strategy minimizes energy consumption in both powertrain and auxiliary components by using predictive information to make informed decisions over a future time horizon.

5.1. Rule-based strategy

The rule-based strategy is illustrated in Fig. 5. The control architecture is divided into three independent domains: air, coolant, and oil flow management. In the airflow control domain, the actuator logic is governed by the radiator coolant outlet temperature, T_{ici}. When T_{ici} is below 65 °C, the AGS remains fully closed ($\phi = 0°$), and the fan is turned off. When $T_{\mathrm{ici}} \geq 65$ °C, the AGS is fully open ($\phi = 90°$), and the fan PWM duty cycle is regulated proportionally to the deviation from the preset 65 °C target. To avoid frequent toggling of the fan, a 10-s hysteresis delay is introduced between transitions.

The coolant flow control domain monitors four component temperatures: winding T_{w}, magnet T_{pm}, inverter junction T_{jt}, and oil cooler outlet T_{emoi}. For each temperature exceeding the preset threshold of 65 °C, the coolant flow request is computed linearly based on the deviation from this target, according to $\dot{V}_{\mathrm{c},i} = f(T_i - 65) + 2\,\mathrm{L\,min^{-1}}$, where $2\,\mathrm{L\,min^{-1}}$ represents the idle flow—i.e., the minimum flow rate required to circulate coolant through the circuit. If the temperature remains below the threshold, the idle flow $\dot{V}_{\mathrm{c},i}$, is maintained at $2\,\mathrm{L\,min^{-1}}$. Among the four individual requests, the maximum is selected to determine the final coolant pump command: $\dot{V}_{\mathrm{c}} = \max(\dot{V}_{\mathrm{c},i})$.

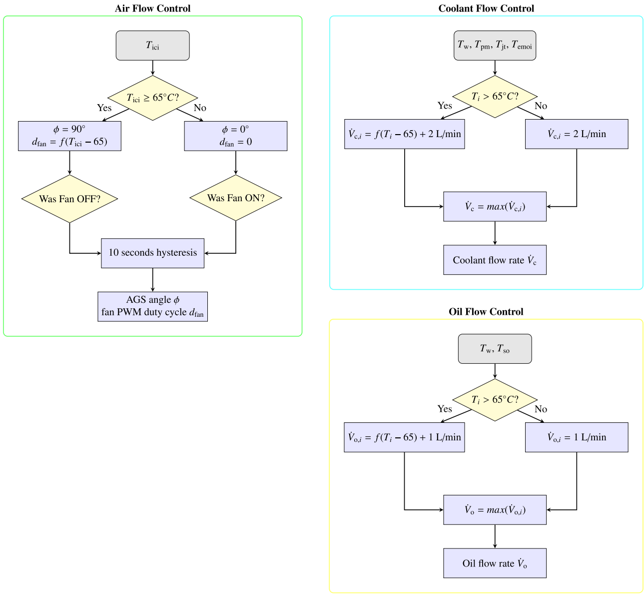

Fig. 5. Rule-based powertrain thermal management strategy.

The oil flow control follows a similar manner as the coolant, regulating flow based on the winding temperature T_{w} and sump oil temperature T_{so}. For each temperature exceeding 65 °C, the requested oil flow is computed as $\dot{V}_{\mathrm{o},i} = k(T_i - 65) + 1\,\mathrm{L\,min^{-1}}$, whereas idle flow $\dot{V}_{\mathrm{o},i} = 1\,\mathrm{L\,min^{-1}}$ is applied otherwise. The final oil pump command is given by the maximum of the two individual requests: $\dot{V}_{\mathrm{o}} = \max(\dot{V}_{\mathrm{o},i})$.

5.2. MPC-based powertrain thermal management

Unlike conventional rule-based strategies that track predefined temperature references, the proposed nonlinear MPC strategy uses a reference-free and economic formulation [46]. Instead of enforcing specific temperature set points, the controller optimizes the actuation of the cooling system to minimize overall energy consumption of the powertrain and its auxiliary components while satisfying physical and safety-related temperature constraints. By leveraging predictive information over a finite time horizon, the MPC proactively balances cooling efforts and temperature-dependent efficiency effects [47].

To this end, a nonlinear OCP is formulated and discretized over a finite horizon N_p. The MPC problem solved at each time step k is given by:

$$
\begin{aligned}
\min_{\{\tilde{u}_k\}_{k=0}^{N_p-1}} \quad & J = \sum_{k=0}^{N_p-1} f_0\left(\tilde{x}_k, \tilde{u}_k\right) \\
\text{s.t.} \quad & \tilde{x}_{k+1} = f\left(\tilde{x}_k, \tilde{u}_k\right), \\
& \tilde{x}_0 = x_0, \\
& x_{\min} \leq \tilde{x}_k \leq x_{\max}, \quad \forall k = 0, \dots, N_p \\
& u_{\min} \leq \tilde{u}_k \leq u_{\max}, \quad \forall k = 0, \dots, N_p - 1
\end{aligned}
\tag{26}
$$

Here, $\tilde{x}_k$ and $\tilde{u}_k$ denote the predicted state and control input at time step k, respectively. The prediction and control horizons are both set to N_p, and the optimization is resolved at every sampling interval.

The cost function minimizes the total electrical energy drawn from the high-voltage battery. The discrete-time stage cost $f_0(k)$ at time step

k is formulated as:

$$f_0(k) = \overbrace{P_{\text{trac}}(k)}^{\text{Traction power}} + \overbrace{P_{\text{ls,w}}(k) + P_{\text{ls,pm}}(k) + P_{\text{ls,inv}}(k) + P_{\text{ls,tran}}(k)}^{\text{Powertrain loss power}} \\ + \overbrace{P_{\text{fan}}(k) + P_{\text{pu,c}}(k) + P_{\text{pu,o}}(k)}^{\text{Cooling power}} \tag{27}$$

The first term, P_{trac}, denotes the mechanical traction power demand at the wheels, determined by the vehicle speed and traction force, and influenced by the AGS angle ϕ through aerodynamic drag and powertrain loading. Positive values of P_{trac} indicate propulsion, where minimization reduces the electrical energy required from the battery. Negative values correspond to regenerative braking, and minimizing this term promotes maximization of the recovered electrical energy through regeneration. The second group of terms represents the temperature-dependent powertrain power loss. Specifically, $P_{\text{ls,w}}$ includes the motor copper losses and stator iron losses, $P_{\text{ls,pm}}$ accounts for the lumped magnet losses and rotor iron losses, whereas $P_{\text{ls,inv}}$ and $P_{\text{ls,tran}}$ denote the inverter and transmission power losses, respectively. The final group captures the electrical power consumption of the cooling actuators, including the radiator fan (P_{fan}), coolant pump ($P_{\text{pu,c}}$), and oil pump ($P_{\text{pu,o}}$). Although these are low-voltage devices, the energy drawn from the high-voltage battery via a DC/DC converter is considered without accounting for conversion losses, owing to the high efficiency of the converter and the relatively low power demand.

The control input vector u consists of the AGS angle ϕ, fan PWM duty cycle d_{fan}, coolant flow rate $\dot{V}_{\text{c}}$, and oil flow rate $\dot{V}_{\text{o}}$, defined as:

$$u = \left[\phi,\ d_{\text{fan}},\ \dot{V}_{\text{c}},\ \dot{V}_{\text{o}}\right] \tag{28}$$

These variables directly govern the convective heat rejection and therefore determine both the cooling power demand and the temperature evolution of the powertrain components.

The state vector x includes the critical temperatures of key powertrain components, as well as the inlet and outlet temperatures of coolant and oil circuits associated with each component. It is expressed as:

$$x = \left[T_{\text{jt}},\ T_{\text{w}},\ T_{\text{pm}},\ T_{\text{ici}},\ T_{\text{ico}},\ T_{\text{emco}},\ T_{\text{emoi}},\ T_{\text{emoo}},\ T_{\text{so}}\right] \tag{29}$$

The system dynamics $f(\tilde{x}_k, \tilde{u}_k)$, which describe the temperature evolution of these components, are detailed in Section 3. It is worth noting that the motor coolant inlet temperature T_{emci} is assumed to be equal to the inverter coolant outlet temperature T_{ico}.

The optimization is subject to physical and safety constraints on both the states and the control inputs. For the states, the following constraints are considered:

- $T_{\text{w}} \leq 180\,°\text{C}$,
- $T_{\text{pm}} \leq 140\,°\text{C}$,
- $T_{\text{jt}} \leq 150\,°\text{C}$,
- $-20 \leq T_{\text{c}} \leq 100\,°\text{C}$,
- $-20 \leq T_{\text{o}} \leq 100\,°\text{C}$.

The temperatures of critical components must remain within operational limits to prevent degradation or failure. The motor winding temperature is limited to below 180 °C, the magnet temperature below 140 °C, and the inverter junction temperature below 150 °C. To avoid fluid phase changes and ensure proper thermal performance, the coolant temperature (EGL 50/50) is maintained between −20 °C and 100 °C, and the oil temperature is also maintained within the same range.

The control inputs are constrained by actuator and system limitations:

- $0 \leq \phi \leq 90°$,
- $0\ \% \leq d_{\text{fan}} \leq 100\ \%$,
- $2\,\text{L}\,\text{min}^{-1} \leq \dot{V}_{\text{c}} \leq 18\,\text{L}\,\text{min}^{-1}$,

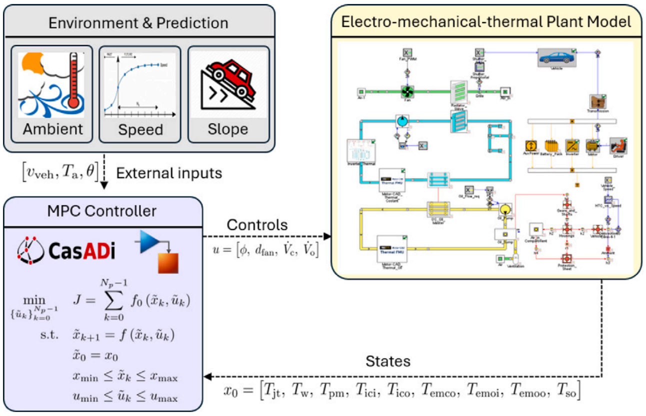

Fig. 6. Implementation of the MPC-based thermal management strategy and its closed-loop interaction with the vehicle and powertrain plant model.

- $1\,\text{L}\,\text{min}^{-1} \leq \dot{V}_{\text{o}} \leq 18\,\text{L}\,\text{min}^{-1}$.

The AGS angle is restricted to 0°- 90°, representing fully closed and fully open positions, respectively. The fan is regulated via a PWM duty cycle, constrained between 0 % and 100 %. The coolant flow rate is bounded between $2\,\text{L}\,\text{min}^{-1}$ and $18\,\text{L}\,\text{min}^{-1}$, whereas the oil flow rate ranges from $1\,\text{L}\,\text{min}^{-1}$ to $18\,\text{L}\,\text{min}^{-1}$, ensuring maintenance of idle flow.

6. Simulation study

6.1. Simulation setup

The study adopts a co-simulation approach using GT-SUITE, Motor-CAD, and Simulink. A comprehensive electro-mechanical–thermal model of the vehicle and powertrain is developed in the GT-SUITE environment, incorporating detailed representations of key powertrain components and their cooling circuits. The electric motor is simulated in Motor-CAD and integrated into GT-SUITE as a functional mock-up unit, allowing for high-fidelity thermal behavior within the system-level simulation.

The MPC-based thermal management strategy is implemented in Simulink and interacts with the plant model in a closed loop. As illustrated in Fig. 6, the MPC controller receives the ambient temperature T_{a}, the predicted vehicle speed profile v_{veh}, and the road slope θ over the prediction horizon as external inputs. It continuously updates relevant temperature states using feedback from the plant model. Based on this information, the controller computes the optimal AGS angle ϕ, fan PWM duty cycle d_{fan}, coolant flow rate $\dot{V}_{\text{c}}$, and oil flow rate $\dot{V}_{\text{o}}$ by solving a nonlinear programming problem using the CasADi optimization toolbox [48] with a sequential quadratic programming solver. The optimal actuation commands are then sent back to the plant model as the control inputs.

6.2. Case study

To evaluate the effectiveness of the proposed thermal management strategies under varying real-world conditions, two routes are studied: one for low-speed urban driving and the other for high-speed highway driving in Gothenburg. The corresponding speed profiles and road grade information for each cycle are shown in Fig. 7.

The urban cycle lasts 5019 s and is characterized by low speeds (mostly below 50 km/h) and frequent stop-and-go traffic. The road grade is dynamic, with multiple steep uphill and downhill segments reaching ±10 %. In contrast, the highway cycle spans 6576 s, beginning with a short rural segment averaging 70 km/h for the first 1000 s, followed by sustained high-speed driving near the speed limit of 110 km/h.

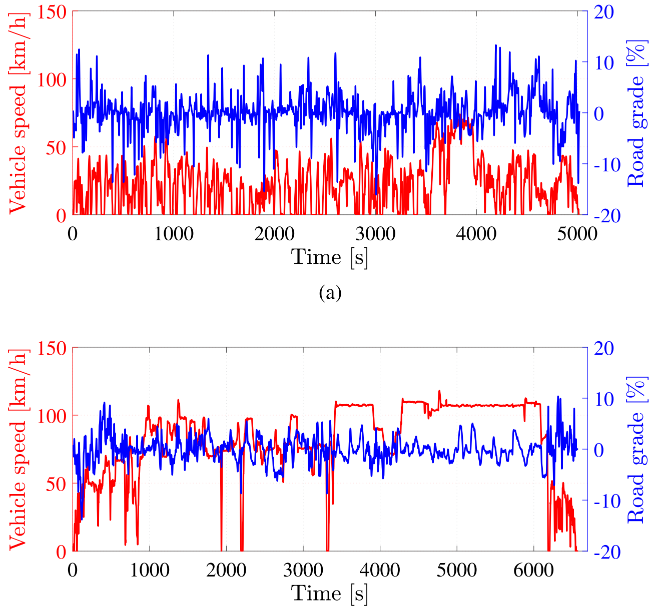

(a)

(b)

Fig. 7. Speed profile and road grade of the representative real-world driving cycles: (a) urban and (b) highway.

Table 2
Battery energy consumption comparison for rule-based and MPC-based thermal management strategies.

Cycle	Rule-based [kWh/100 km]	MPC-based [kWh/100 km]	Diff [%]
Urban	15.36	15.32	−0.26
Highway	20.85	20.63	−1.06

The highway portion has a relatively smooth road grade with minimal variation. For this study, the ambient temperature is set at 23 °C, and the vehicle is assumed to be fully thermally soaked to this temperature prior to departure.

6.3. Simulation result

The battery energy consumption for the urban and highway cycles under rule-based and MPC-based thermal management strategies is summarized in Table 2. The results indicate that the MPC-based strategy reduces battery energy consumption compared to the rule-based strategy in both driving cycles. The urban cycle shows a marginal reduction of 0.26 % is observed, while the highway cycle achieves a more significant saving of 1.06 %. A detailed breakdown of energy usage differences between the rule-based and MPC-based strategies, categorized into auxiliary component consumption, powertrain losses, and aerodynamic energy losses, is shown in Fig. 8.

Urban cycle: Fig. 9 illustrates the comparison of control commands and key component temperatures under MPC-based and rule-based strategies during the urban cycle. Both strategies maintain powertrain component temperatures within safe limits. However, owing to the low-speed and low-power nature of the urban cycle, thermal stress is minimal, resulting in all component temperatures remaining well below their upper bounds.

The MPC-based strategy relies on AGS instead of the fan to increase airflow through the radiator. At low speeds, aerodynamic drag is negligible, so the increased AGS opening has minimal impact on energy consumption. The fan is not used under the MPC-based strategy, whereas the rule-based strategy activates the fan occasionally after 3000 s along with a fully opened AGS. In contrast, the MPC strategy employs partial but more frequent AGS openings, resulting in energy savings of 2.03 Wh from aerodynamic drag and 0.53 Wh from the fan.

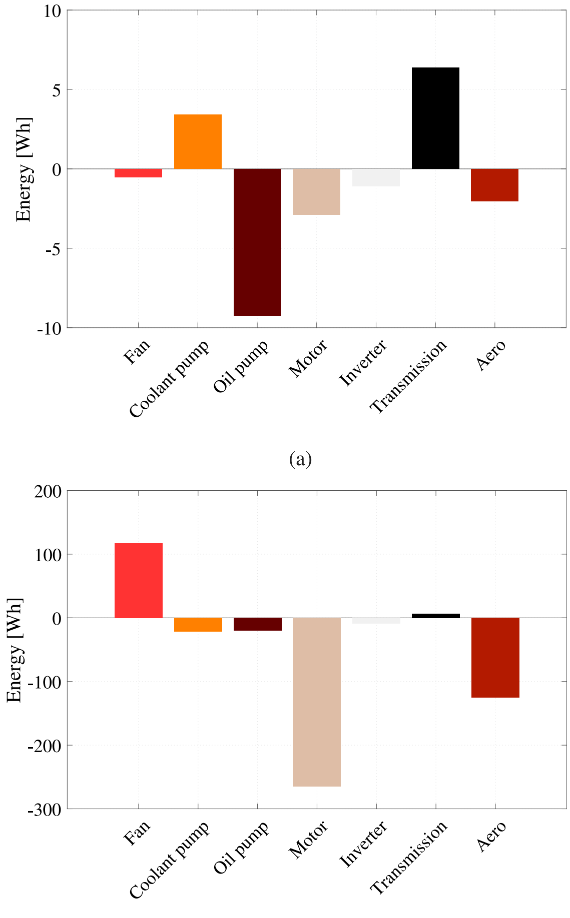

(a)

(b)

Fig. 8. Breakdown of energy usage difference between rule-based and MPC-based thermal management strategies: (a) urban cycle and (b) highway cycle.

In the rule-based strategy, no active cooling occurs during the first 2000 s, as the target threshold of 65 °C is not reached. In contrast, the MPC-based strategy initiates active cooling earlier by increasing the coolant flow rate. This results in slightly lower powertrain component temperatures and an increase in coolant pump energy consumption of 3.43 Wh. Reduced inverter and motor temperatures contribute to lower power losses, yielding savings of 1.09 Wh and 2.89 Wh, respectively. These savings result from reduced current demand due to enhanced magnet strength with cooler magnets under the maximum-torque-per-ampere control strategy, as well as temperature-dependent reductions in motor winding resistance, semiconductor on-state resistance, and switching energy [44,49]. Furthermore, the MPC-based strategy maintains the oil pump at idle flow for almost the entire cycle, resulting in a 9.25 Wh reduction in oil pump energy. The coolant loop can sufficiently handle the thermal load under mild urban driving conditions and is more energy-efficient than the oil circuit, which operates at higher pumping pressure. Conversely, the transmission experiences a 6.37 Wh

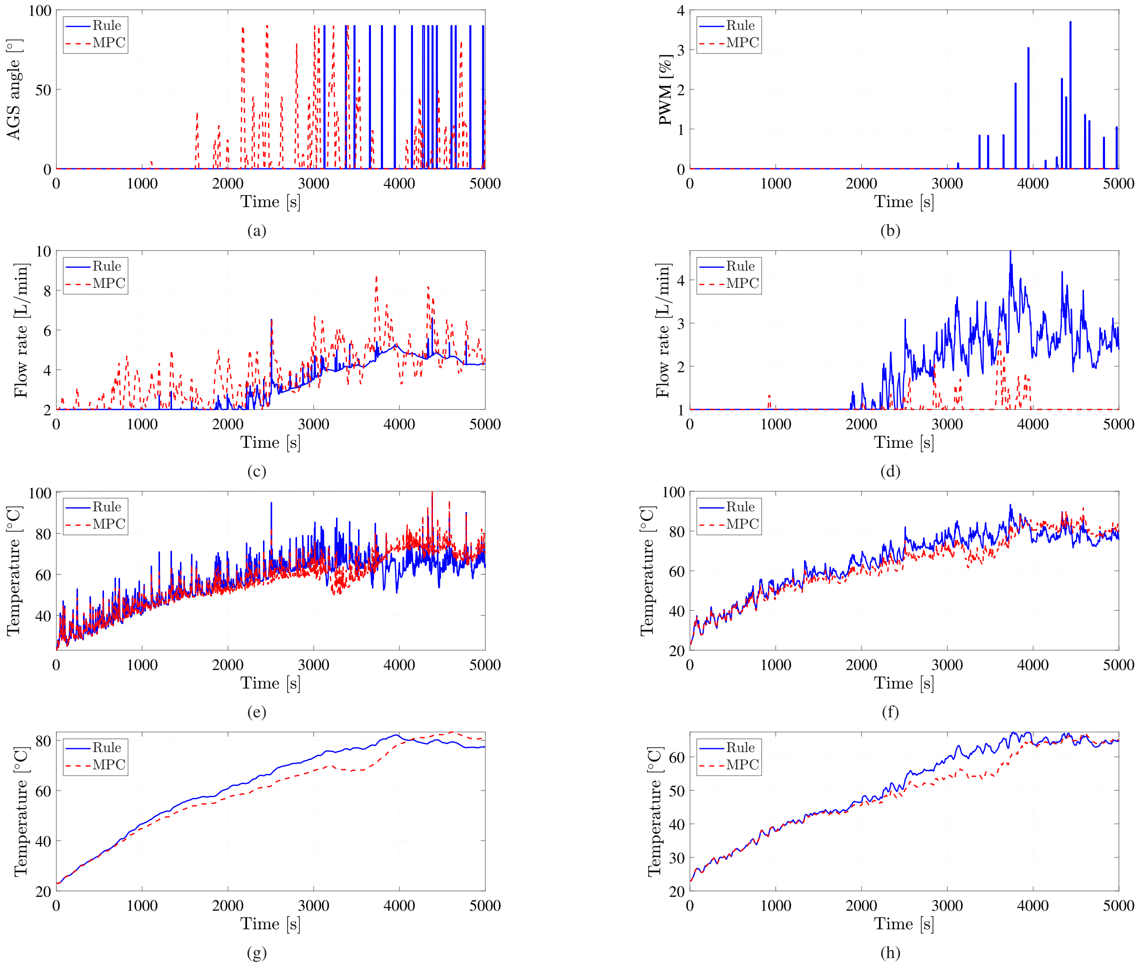

(a) (b) (c) (d) (e) (f) (g) (h)

Fig. 9. Comparison between rule-based and MPC-based thermal management strategies for the urban cycle: (a) AGS angle, (b) fan PWM duty cycle, (c) coolant flow rate, (d) oil flow rate, (e) inverter junction temperature, (f) motor winding temperature, (g) motor magnet temperature, and (h) transmission sump oil temperature.

increase in losses under the MPC-based strategy. For the studied transmission, efficiency follows a parabolic relationship with oil temperature, peaking approximately at 80 °C. Operating below this optimal temperature leads to increased losses due to higher oil viscosity.

The MPC-based strategy results in higher coolant pump energy consumption and increased transmission losses, offset by greater savings in inverter and motor losses, oil pump usage, and aerodynamic drag. This leads to a modest 0.26 % reduction in battery energy consumption over the urban cycle, consistent with the low power demand and limited thermal stress characteristic of mild driving conditions. The results indicate that under urban driving conditions, transmission losses and associated oil pump energy consumption significantly affect thermal management optimization. Specifically, oil pump energy reduction and increased transmission losses yield a net contribution of 2.88 Wh toward energy reduction. However, when excluding the oil pump and transmission losses, the remaining energy terms reflect a net reduction of 3.13 Wh, comparable to the transmission-oil pump contribution. This demonstrates that the transmission and oil circuit play a critical role in optimizing integrated powertrain thermal management. Consequently, MPC-based thermal management strategies developed without considering the transmission may not fully exploit potential energy savings under low-speed operating conditions.

Highway cycle: Fig. 10 shows the details and comparison of the control commands and key component temperatures under MPC-based and rule-based strategies during the highway cycle. The highway cycle involves high-speed, high-power operation, resulting in greater thermal stress on powertrain thermal management compared to the low-speed, low-power urban cycle. Consequently, powertrain component temperatures are significantly higher in both rule-based and MPC-based strategies. The MPC-based strategy permits components to operate closer to their thermal limits, with motor winding, magnet, and transmission sump oil temperatures nearing their upper bounds, and the inverter junction temperature reaching its limit approximately at 2000 s.

In the rule-based strategy, a strong cooling effort is evident, characterized by frequent fully opened AGS angles but limited fan activation. In contrast, the MPC-based strategy features fewer AGS openings, applying increased fan usage in the later stages of the cycle where accumulated thermal stress becomes critical. Given the high vehicle speeds during highway driving, natural airflow through the AGS is more effective, favoring the rule-based strategy. However, this results in higher aerodynamic drag, with 125.22 Wh consumed versus 117.19 Wh in the MPC-based strategy. Thus, in high-speed scenarios, it may be more energy-efficient to use fans with partially open AGS rather than fully opening the AGS, as aerodynamic drag has a stronger impact.

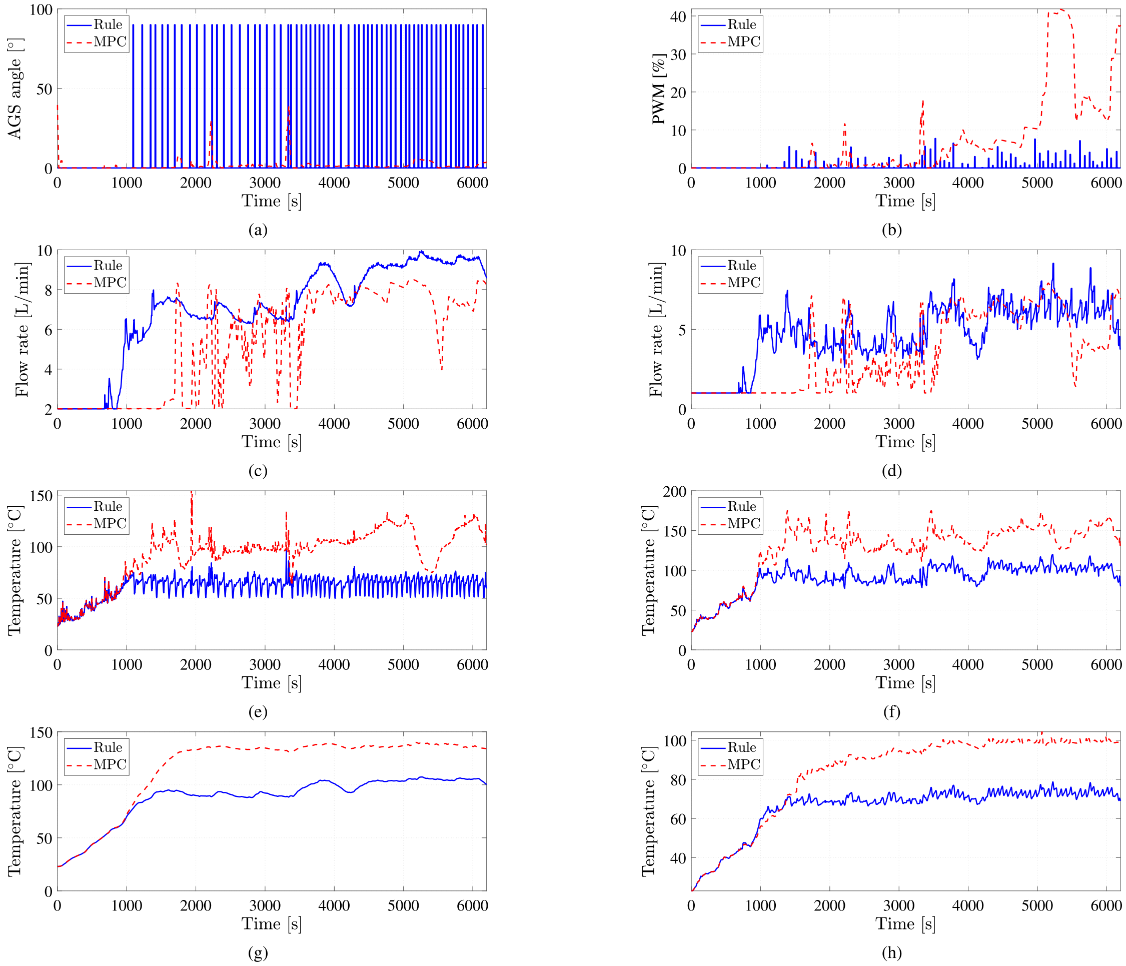

Fig. 10. Comparison between rule-based and MPC-based thermal management strategies for the highway cycle: (a) AGS angle, (b) fan PWM duty cycle, (c) coolant flow rate, (d) oil flow rate, (e) inverter junction temperature, (f) motor winding temperature, (g) motor magnet temperature, and (h) transmission sump oil temperature.

Furthermore, both coolant and oil flow rates are generally lower in the MPC-based strategy, and active cooling starts much later at approximately 2000 s compared to 800 s in the rule-based strategy. At this point, powertrain component temperatures are nearing their upper limits: the magnet reaches 140 °C, the transmission sump oil approaches 100 °C, the inverter junction hovers approximately at 100 °C, and the motor winding reaches 150 °C. Conversely, the rule-based strategy implements conservative cooling, maintaining lower component temperatures: inverter junction at 70 °C, motor winding at 100 °C, magnet at 100 °C, and transmission sump oil at approximately 75 °C, after an initial warm-up phase. This approach leads to higher auxiliary energy consumption, with 21.36 Wh and 19.99 Wh used for the coolant and oil pumps, respectively. The elevated operating temperatures under the MPC-based strategy yield the opposite effect compared to the urban cycle regarding powertrain losses. During highway driving, vehicle speed exceeds 100 km/h, corresponding to motor speeds above 8000 rpm, entering the field weakening region for the studied IPMSM. The increased magnet temperature reduces its strength, thereby requiring less demagnetizing current. Despite higher winding resistance, semiconductors' on-state resistance and switching energy due to elevated temperatures, the inverter and motor losses are reduced by 9.01 Wh and 264.61 Wh as an overall result, respectively. The MPC-based strategy effectively utilizes the full thermal operating range of powertrain components, leveraging predictive information to maximize thermal margins and minimize cooling efforts. This reduces auxiliary energy use and component losses, resulting in a significant 1.06 % reduction in battery energy consumption over the highway cycle, consistent with the high power and thermal demand of this driving condition.

Additionally, the sump oil temperature in the MPC-based strategy is slightly above the optimal level, whereas it is slightly below in the rule-based strategy. Consequently, the transmission experiences marginally higher losses in the MPC case, with an increase of 6.5 Wh compared to the rule-based approach. In the highway cycle, overall energy reduction is primarily driven by motor loss reduction, unlike the urban cycle. The MPC-based strategy intentionally regulates the transmission sump oil temperature near its upper limit of 100 °C to enhance motor efficiency. Without explicitly modeling the integrated oil-cooled transmission, high-temperature operation could risk transmission overheating. Thus, incorporating the transmission and oil circuit is essential to fully leverage temperature-dependent motor efficiency benefits under highway driving conditions.

7. Powertrain component lifetime

Section 6 demonstrated that the MPC-based thermal management strategy significantly improves energy efficiency, particularly under high-speed driving conditions. However, this is achieved by more aggressively utilizing the available thermal margins of the powertrain, resulting in elevated operating temperatures of critical components. Although this operation benefits energy efficiency, it raises concerns about the durability of powertrain components from a thermal perspective. Faster thermal aging, resulting from sustained high temperatures and repeated thermal cycling, accelerates the degradation of materials and interfaces, ultimately leading to premature failure and a shortened component lifetime.

This section examines the effect of the MPC-based thermal management strategy on the lifespan of key powertrain components, with a focus on the inverter and electric motor, which are the most thermally stressed and prone to failure in electric powertrains [50]. First, lifetime estimation models for the inverter and motor are introduced. The influence of the MPC-based strategy on component lifetime is then evaluated under urban, highway, and real-world mixed driving conditions.

7.1. Inverter lifetime estimation

In power semiconductor modules, the primary thermally induced failure mechanisms are bond-wire degradation and solder fatigue, both driven by temperature-induced mechanical stress [51]. A rainflow counting method [52] is employed to convert the randomly varying thermal loading profiles into standardized thermal cycles suitable for lifetime modeling. This method extracts key metrics including the junction temperature variation ΔT_{jt}, mean junction temperature $T_{\mathrm{jt,m}}$ and the number of thermal cycles.

Based on the semiconductor lifetime prediction model in [53,54], the damage accumulation D in the power semiconductor is calculated using Miner's rule [55], which sums the ratio of the number of cycles N_i experienced at a specific junction temperature swing to the corresponding number of cycles to failure N_{f_i} determined by the lifetime model:

$$D = \sum_i \frac{N_i}{N_{f_i}} \tag{30}$$

The expected lifetime LF can be estimated based on the accumulated damage D induced by temperature cycling over a defined trip duration t_{trip} as:

$$LF = \frac{t_{\mathrm{trip}}}{D} \tag{31}$$

7.2. Motor lifetime estimation

In electric motors, the primary thermally induced failure mechanism is the degradation of insulation materials [35,56]. Elevated winding temperatures accelerate the aging of insulation by increasing the rate of chemical and physical degradation processes. This is modeled using Arrhenius-based formulations, where insulation lifetime decreases exponentially with rising temperature. The lifetime loss fraction (LLF) of winding insulation under a time-varying temperature profile can be calculated using the Arrhenius–Dakin model as [57]:

$$LLF = \int_0^{t_{\mathrm{trip}}} \frac{1}{LF_{\mathrm{ref}} \cdot \exp\left[B\left(\frac{1}{T(t)} - \frac{1}{T_{\mathrm{ref}}}\right)\right]}\, dt \tag{32}$$

For Class H insulation, commonly used in electric motors, the reference lifetime is $LF_{\mathrm{ref}} = 20\,000\,\mathrm{h}$ at a reference temperature $T_{\mathrm{ref}} = 180\,^{\circ}\mathrm{C}$. The overall lifetime over the defined trip can then be estimated as:

$$LF = \frac{t_{\mathrm{trip}}}{LLF} \tag{33}$$

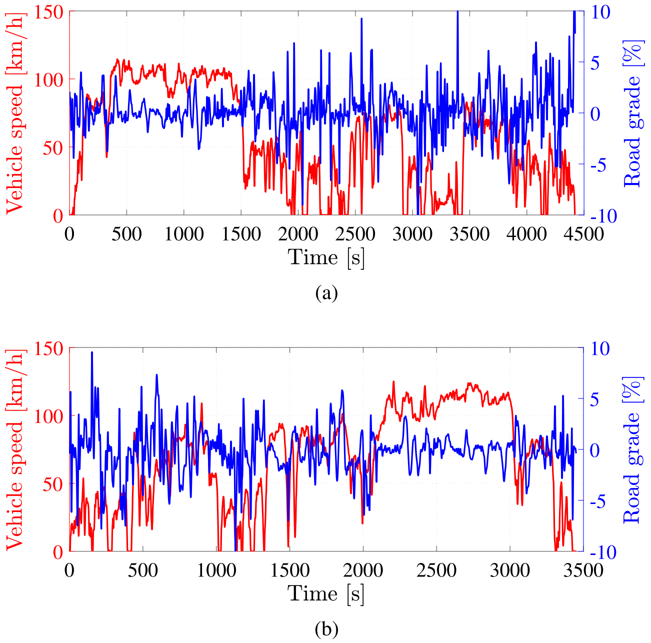

(a)

(b)

Fig. 11. Speed profile and road grade of the round-trip: (a) STEN to GBG and (b) GBG to STEN.

Table 3
Inverter and motor lifetime over different driving cycles under rule-based and MPC-based thermal management strategies.

Component	Cycle	Rule-based [h]	MPC-based [h]	Change [%]
Inverter	Urban	4.35×10^5	5.50×10^5	+26.3
	Highway	5.64×10^5	6.25×10^4	−88.9
	Round-trip	5.41×10^4	1.01×10^4	−81.3
Motor	Urban	2.66×10^7	2.96×10^7	+11.4
	Highway	3.48×10^6	1.61×10^5	−95.4
	Round-trip	4.81×10^5	2.01×10^4	−95.8

7.3. Influence of MPC-based strategy on component lifetime

In addition to the pure urban and highway driving cycles described in Section 6, a real-world round-trip commute route between Stenungsund (STEN) and Gothenburg (GBG) is analyzed to assess component degradation under mixed driving conditions. This route features highway, rural, and urban segments with an approximate one-way distance of 66 km, representing a typical daily BEV usage pattern. The speed profiles and road grades in both directions are shown in Fig. 11.

Table 3 lists the estimated lifetimes of the inverter and motor for the three driving cycles, utilizing both rule-based and MPC-based thermal management strategies. The results demonstrate the strong sensitivity of inverter and motor lifetimes to driving conditions when the MPC-based strategy is applied.

Under urban driving, the MPC-based strategy increases the lifetimes of both the inverter and motor by approximately 26 % and 11 %, respectively. This improvement is attributed to enhanced cooling at low speeds, resulting in lower average temperatures at the inverter junction and motor windings. As shown in Fig. 9, this operating behavior benefits both energy efficiency and component durability under urban conditions. Additionally, the MPC-based strategy reduces temperature fluctuations of the inverter junction, further minimizing accumulated thermal damage.

In contrast, under sustained highway operation, the MPC-based strategy drastically reduces the inverter lifetime by approximately 89 % and the motor lifetime by more than 95 %. This severe degradation

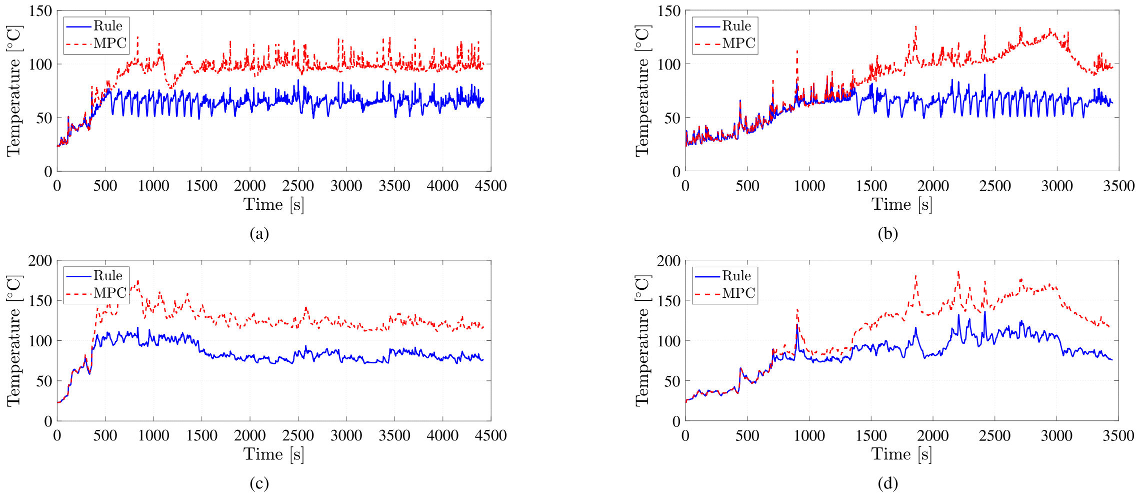

Fig. 12. Comparison of inverter junction temperature and motor winding temperature over the round-trip commute route under rule-based and MPC-based thermal management strategies: (a) inverter STEN to GBG, (b) inverter GBG to STEN, (c) motor STEN to GBG, and (d) motor GBG to STEN.

arises from the aggressive exploitation of thermal margins in the high-speed field-weakening operating region, where elevated operating temperatures dominate the aging process (Fig. 10). Although the MPC-based strategy maintains smoother inverter temperature profiles with reduced thermal cycling, the higher average junction temperature outweighs the benefits of reduced temperature fluctuations. This explains why the inverter's relative lifetime deterioration is less severe than that of the motor under MPC-based operation.

For the real-world round-trip commuting route, which includes urban, rural, and highway driving, the lifetimes of the inverter and motor are reduced by approximately 81 % and 96 %. Fig. 12 shows the inverter junction temperature and motor winding temperature during the round-trip commute under both rule-based and MPC-based thermal management strategies. When traveling from STEN to GBG, the drive begins with a highway segment, leading to elevated component temperatures early in the cycle. Even during the later urban section, the MPC-based strategy maintains high temperatures, as strong cooling would yield only a marginal reduction in powertrain loss. Conversely, in the GBG to STEN direction, the drive starts with an urban segment, where the MPC-based strategy initially behaves similarly to the pure urban cycle. However, this advantage is soon negated by the subsequent highway section, resulting in elevated temperatures again. Overall, highway operation dominates lifetime degradation in both cases.

These results demonstrate that the MPC-based thermal management strategy can be beneficial or detrimental to component lifetime, depending on the operating regime. Although favorable lifetime behavior may occur under low-speed urban driving conditions, the same strategy can lead to critical aging under sustained highway or mixed real-world driving.

For the representative real-world round-trip commute route, the inverter exhibits a shorter lifetime than the motor, and therefore becomes the lifetime-limiting component of the powertrain. Under the MPC-based strategy, the estimated inverter lifetime is reduced by 81 % compared to the rule-based strategy, corresponding to a projected driving distance of 608 290 km versus 3 267 300 km. Despite this reduction, the inverter lifetime under MPC-based thermal management exceeds the typical BEV component warranty requirements, which are generally approximately 300 000 km [58,59]. Thus, even with the increased thermal stress from the MPC-based strategy, the inverter's projected lifetime remains feasible under realistic usage conditions.

8. Conclusion and future work

This study proposed an MPC-based thermal management strategy for an electric powertrain with a mixed coolant/oil cooling architecture. The controller uses a control-oriented model to minimize overall battery energy consumption by optimally balancing auxiliary cooling energy (fan and pumps) and temperature-dependent powertrain losses (inverter, electric motor, and transmission).

Simulation results show that the MPC-based strategy reduces battery energy consumption by 0.26 % in a low-speed urban cycle and 1.06 % in a high-speed highway cycle. Improvements are pronounced in the highway cycle, where increased aerodynamic drag and thermal stress create greater optimization potential. The results further reveal that, under urban driving conditions, the transmission and oil circuit form a previously overlooked but critical contributor to the net energy balance, whereas under highway driving, the energy savings are dominated by motor loss reduction enabled by elevated operating temperatures, but constrained by the oil temperature and the corresponding efficiency characteristics of the transmission.

To assess the long-term implications, the thermal durability of the inverter and electric motor was systematically evaluated under urban driving, highway driving, and a real-world round-trip commute route scenario representing a typical BEV usage pattern. The results indicate that the impact of MPC-based thermal management on component lifetime is sensitive to the driving profile. Although the MPC strategy improves component lifetime under low-speed urban driving, it causes significant lifetime degradation during sustained high-speed operation due to aggressive use of thermal margins. However, in real-world commuting scenarios, the projected powertrain lifetime remains above typical BEV warranty requirements, even with the MPC-based strategy.

In conclusion, the proposed MPC-based thermal management strategy offers a promising solution for improving BEV energy efficiency and utilizing the full thermal operating range of integrated powertrain components. The results indicate that energy optimization and component lifetime are intrinsically coupled and must be jointly considered. Future work will focus on lifetime-aware MPC formulations, embedding physically based aging models directly into the optimization objective to enable a balanced, application-dependent trade-off between energy efficiency and long-term durability. Additionally, the proposed strategy will be extended to encompass complete vehicle thermal management by integrating the battery thermal system and cabin, allowing for unified optimization of powertrain efficiency, battery aging, and passenger comfort.

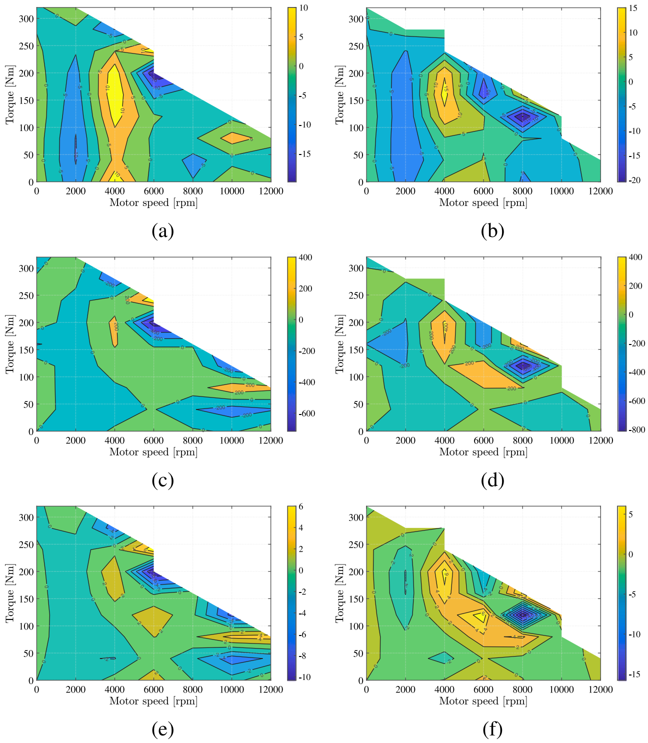

Fig. A.13. Contour plots of the absolute fitting error for: (a,b) phase current I_p, (c,d) motor winding node loss $P_{\mathrm{ls,w}}$, and (e,f) motor magnet node loss $P_{\mathrm{ls,pm}}$. Left: $T_{\mathrm{w}} = 80$ °C, $T_{\mathrm{pm}} = 75$ °C; Right: $T_{\mathrm{w}} = 160$ °C, $T_{\mathrm{pm}} = 150$ °C.

CRediT authorship contribution statement

Y. Xu: Writing – original draft, Visualization, Software, Methodology, Formal analysis, Conceptualization. **S. Klacar:** Writing – review & editing, Supervision, Formal analysis. **S. George:** Methodology, Data curation. **A. Andersson:** Methodology, Data curation. **D. Sedarsky:** Writing – review & editing, Supervision. **A. Kersten:** Writing – review & editing.

Declaration of Generative AI and AI-assisted technologies in the writing process

None

Declaration of competing interest

The authors declare that they have no known competing financial interests or personal relationships that could have appeared to influence the work reported in this paper.

Acknowledgment

This work was supported by the Swedish Energy Agency program for vehicle research and innovation (FFI), grant number P2024-01000.

Appendix A. Validation of the fitted maps

See Figs. A.13 and A.14.

Appendix B. Validation of control-oriented thermal model

See Figs. B.15 and B.16 and Table B.4.

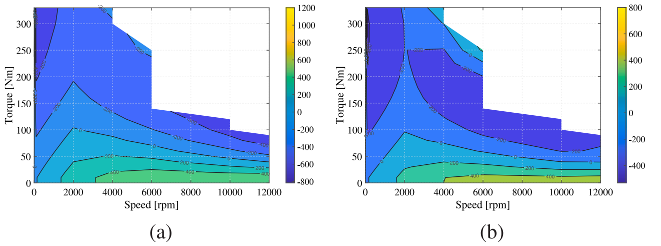

Fig. A.14. Contour plots of the absolute fitting error for the transmission loss $P_{\mathrm{ls,tran}}$ under different sump oil temperature conditions: (a) $T_{\mathrm{so}} = 60$ °C and (b) $T_{\mathrm{so}} = 100$ °C.

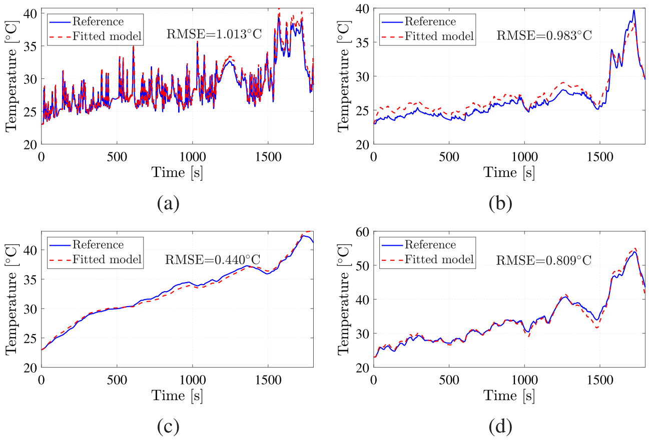

Fig. B.15. Validation of the control-oriented model against the high-fidelity GT-SUITE reference model for key powertrain node temperatures under WLTC with fully open shutter, $T_{\mathrm{a}} = 23\,°\mathrm{C}$, coolant flow rate $\dot{V}_{\mathrm{c}} = 6\,\mathrm{L\,min^{-1}}$, and oil flow rate $\dot{V}_{\mathrm{o}} = 6\,\mathrm{L\,min^{-1}}$: (a) inverter junction temperature T_{jt}, (b) motor winding temperature T_{w}, (c) motor magnet temperature T_{pm}, (d) transmission sump oil temperature T_{so}.

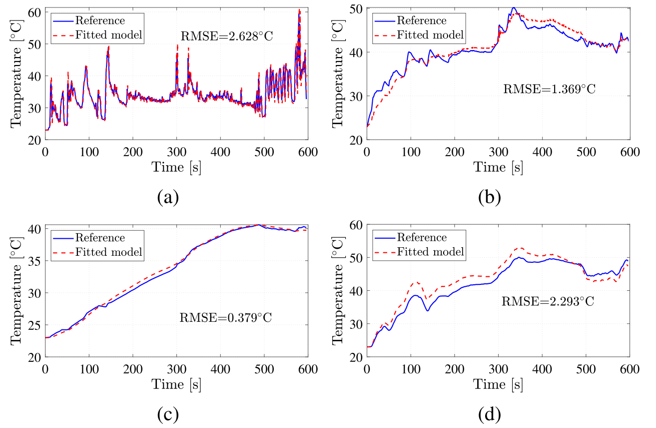

Fig. B.16. Validation of the control-oriented model against the high-fidelity GT-SUITE reference model for key powertrain node temperatures under US06 with fully open shutter, $T_{\mathrm{a}} = 23\,°\mathrm{C}$, coolant flow rate $\dot{V}_{\mathrm{c}} = 6\,\mathrm{L\,min^{-1}}$, and oil flow rate $\dot{V}_{\mathrm{o}} = 6\,\mathrm{L\,min^{-1}}$: (a) inverter junction temperature T_{jt}, (b) motor winding temperature T_{w}, (c) motor magnet temperature T_{pm}, (d) transmission sump oil temperature T_{so}.

Data availability

Data will be made available on request.

Table B.4
RMSE of key powertrain node temperatures under WLTC and US06 for different coolant ($\dot{V}_c$) and oil ($\dot{V}_o$) flow rates.

Drive cycle	Node	Oil flow rate $\dot{V}_o$	Coolant flow rate $\dot{V}_c$	
			2	6
WLTC	Inverter junction temp. T_{jt}	2	0.987	0.964
		6	0.987	1.013
	Motor winding temp. T_w	2	1.749	1.440
		6	1.998	0.983
	Motor magnet temp. T_{pm}	2	0.982	0.648
		6	1.762	0.440
	Sump oil temp. T_{so}	2	1.805	1.581
		6	1.227	0.809
US06	Inverter junction temp. T_{jt}	2	2.615	2.623
		6	2.623	2.628
	Motor winding temp. T_w	2	1.922	2.741
		6	1.237	1.369
	Motor magnet temp. T_{pm}	2	1.264	0.833
		6	0.785	0.379
	Sump oil temp. T_{so}	2	2.260	2.849
		6	2.485	2.293

References

[1] J. Buberger, A. Kersten, M. Kuder, R. Eckerle, T. Weyh, T. Thiringer, Total CO2-equivalent life-cycle emissions from commercially available passenger cars, Renew. Sustain. Energy Rev. 159 (2022) 112158.

[2] A. García, J. Monsalve-Serrano, S. Martinez-Boggio, S. Tripathi, Techno-economic assessment of vehicle electrification in the six largest global automotive markets, Energy Convers. Manage. 270 (2022) 116273.

[3] A. Pamidimukkala, S. Kermanshachi, J.M. Rosenberger, G. Hladik, Barriers and motivators to the adoption of electric vehicles: A global review, Green Energy Intell. Transp. 3 (2) (2024) 100153.

[4] B.N. Alhasnawi, M. Zanker, V. Bureš, A new smart charging electric vehicle and optimal DG placement in active distribution networks with optimal operation of batteries, Results Eng. 25 (2025) 104521.

[5] B.N. Alhasnawi, H.K. Hashim, M. Zanker, V. Bureš, The rising, applications, challenges, and future prospects of energy in smart grids and smart cities systems, Energy Convers. Manag.: X (2025) 101162.

[6] Y. Al-Wreikat, C. Serrano, J.R. Sodré, Effects of ambient temperature and trip characteristics on the energy consumption of an electric vehicle, Energy 238 (2022) 122028.

[7] J. Seo, R. Vijayagopal, N. Kim, A. Rousseau, K. Stutenberg, Effects of ambient temperature on electric vehicle range considering battery performance, powertrain Efficiency, and HVAC load, Energy Convers. Manage. 326 (2025) 119493.

[8] Y. Yang, B. Bilgin, M. Kasprzak, S. Nalakath, H. Sadek, M. Preindl, J. Cotton, N. Schofield, A. Emadi, Thermal management of electric machines, IET Electr. Syst. Transp. 7 (2) (2017) 104–116.

[9] A. Al-Timimy, P. Giangrande, M. Degano, M. Galea, C. Gerada, Investigation of AC copper and iron losses in high-speed high-power density PMSM, in: 2018 XIII International Conference on Electrical Machines, ICEM, IEEE, 2018, pp. 263–269.

[10] L. Liu, Y. Guo, G. Lei, J. Zhu, Comparative iron loss analysis of the interior PMSMs for electric vehicles considering the effects of temperature variation, in: 2023 IEEE International Conference on Applied Superconductivity and Electromagnetic Devices, ASEMD, IEEE, 2023, pp. 1–2.

[11] D.P. Nayak, R.K. Yakala, M. Kumar, S.K. Pramanick, Temperature-dependent reverse recovery characterization of SiC MOSFETs body diode for switching loss estimation in a half-bridge, IEEE Trans. Power Electron. 37 (5) (2021) 5574–5582.

[12] F. Jiang, K. Sheng, Q. Guo, Comparative study of temperature-dependent characteristics for SiC MOSFETs, in: 2016 13th China International Forum on Solid State Lighting: International Forum on Wide Bandgap Semiconductors China, SSLChina: IFWS, IEEE, 2016, pp. 50–53.

[13] D. Jiang, R. Burgos, F. Wang, D. Boroyevich, Temperature-dependent characteristics of SiC devices: Performance evaluation and loss calculation, IEEE Trans. Power Electron. 27 (2) (2011) 1013–1024.

[14] S. Yan, Z. Kong, H. Liu, L. Zhang, X. Hu, Y. Hou, Power loss evaluation of an E-axle gearbox considering the influence of gear oil factors, Lubricants 12 (1) (2024) 11.

[15] İ. Kaya, C. Baykara, The investigation of the effect of operating conditions in gearboxes on efficiency, Adv. Mech. Eng. 16 (4) (2024) 16878132241248072.

[16] J. Xu, C. Zhang, R. Fan, H. Bao, Y. Wang, S. Huang, C.S. Chin, C. Li, Modelling and control of vehicle integrated thermal management system of PEM fuel cell vehicle, Energy 199 (2020) 117495.

[17] D. Li, C. Zhang, R. Fan, L. Xu, Y. Wang, W. Guo, J. Chen, M. Ni, An innovative thermal management method for cooling loop of electric driving system for durable and high efficiency electric vehicle, Appl. Therm. Eng. 195 (2021) 117176.

[18] T. Bächle, K. Graichen, M. Buchholz, K. Dietmayer, Loss-focused predictive thermal management of induction motors in electric vehicles using nonlinear fixed-point MPC, in: 2016 IEEE Conference on Control Applications, CCA, IEEE, 2016, pp. 1392–1397.

[19] M. Ghazali, M. Vukotić, D. Miljavec, A.E. Hartavi, Temperature-adaptive torque allocation for all wheel drive electric trucks, Appl. Therm. Eng. (2025) 126846.

[20] L. Guo, B. Yang, J. Ye, Predictive energy management for dual-motor BEVs considering temperature-dependent traction inverter loss, IEEE Trans. Transp. Electrification 8 (1) (2021) 1501–1515.

[21] X. Tao, K. Zhou, J.R. Wagner, H. Hofmann, An electric motor thermal management system for hybrid vehicles: modelling and control, Int. J. Veh. Perform. 2 (3) (2016) 207–227.

[22] X. Wang, Y. Feng, Research on energy consumption optimization control strategy of electric vehicle electric drive oil/water cooling system, Int. J. Automot. Technol. 25 (3) (2024) 595–610.

[23] S.S. Naini, R.S. Miller, D. Rizoo, J. Wagner, A model reference adaptive controller for an electric motor thermal management system in autonomous vehicles, SAE Int. J. Electrified Veh. 12 (1) (2023) 3–16.

[24] S. Yu, C. Haspolat, Y. Yalcin, S. Msaddi, B. Chen, S.A. Evangelou, I.M. Jaimoukha, Motor-temperature-aware optimal energy management for dual-motor electric buses, in: 2024 IEEE Vehicle Power and Propulsion Conference, VPPC, IEEE, 2024, pp. 1–6.

[25] S. Schaut, E. Arnold, O. Sawodny, Predictive thermal management for an electric vehicle powertrain, IEEE Trans. Intell. Veh. 8 (2) (2021) 1957–1970.

[26] A. Wahl, C. Wellmann, B. Krautwig, P. Manns, B. Chen, C. Schernus, J. Andert, Efficiency increase through model predictive thermal control of electric vehicle powertrains, Energies 15 (4) (2022) 1476.

[27] A. Wahl, C. Wellmann, C. Monissen, J. Andert, Active temperature control of electric drivetrains for efficiency increase, Appl. Energy 338 (2023) 120887.

[28] C. Wellmann, A.R. Khaleel, T. Brinkmann, A. Wahl, C. Monissen, M. Eisenbarth, J. Andert, Electric machine co-optimization for EV drive technology development: Integrating Bayesian optimization and nonlinear model predictive control, ETransportation 23 (2025) 100392.

[29] P. Janssen, G. Hellenbroich, H.-P. Lahey, Highly integrated electric drive unit for passenger cars, ATZ Worldw. 120 (11) (2018) 52–55.

[30] R. Wrobel, A technology overview of thermal management of integrated motor drives–Electrical Machines, Therm. Sci. Eng. Prog. 29 (2022) 101222.

[31] L. Pointner-Gabriel, T. Franzelin, B. Morhard, D. Schweigert, K. Voelkel, K. Stahl, Electric drive units: A set-up for investigating function, efficiency, and dynamics, Vehicles 6 (3) (2024) 1415–1441.

[32] M.H. Park, E.J. Manalac, S.C. Kim, Evaluating hybrid cooling in in-wheel motors with reduction gear for electric vehicles, Int. J. Automot. Technol. (2025) 1–11.

[33] J.F. Shore, A. Kadiric, Optimisation of electric vehicle drivetrain fluid with a new system-level approach, Tribol. Trans. (2025) 1–22.

[34] M. Thoben, F. Sauerland, K. Mainka, S. Edenharter, L. Beaurenaut, Lifetime modeling and simulation of power modules for hybrid electrical/electrical vehicles, Microelectron. Reliab. 54 (9–10) (2014) 1806–1812.

[35] R. Rothe, K. Hameyer, Life expectancy calculation for electric vehicle traction motors regarding dynamic temperature and driving cycles, in: 2011 IEEE International Electric Machines & Drives Conference, IEMDC, IEEE, 2011, pp. 1306–1309.

[36] B. Chen, C. Wulff, K. Etzold, P. Manns, G. Birmes, J. Andert, S. Pischinger, A comprehensive thermal model for system-level electric drivetrain simulation with respect to heat exchange between components, in: 2020 19th IEEE Intersociety Conference on Thermal and Thermomechanical Phenomena in Electronic Systems, ITherm, IEEE, 2020, pp. 558–567.

[37] A. Bourgault, O. Taqavi, Z. Li, G. Byczynski, N.C. Kar, Advanced lumped parameter thermal network for modeling of cooling solutions in electric vehicle motor applications, IEEE Trans. Magn. (2024).

[38] S. Amirpour, R. Orbay, T. Thiringer, M.K. Samani, G. Mademlis, D. Larsson, A. Andersson, Highly thermal conductive graphene-based heatsink tailored for electric propulsion SiC-based inverter, Appl. Therm. Eng. 243 (2024) 122548.

[39] A. Wintrich, U. Nicolai, W. Tursky, T. Reimann, Application Manual Power Semiconductors, vol. 2, ISLE Verlag Ilmenau, Germany, 2015.

[40] J. Durand de Gevigney, C. Changenet, F. Ville, P. Velex, Thermal modelling of a back-to-back gearbox test machine: Application to the FZG test rig, Proc. Inst. Mech. Eng. Part J: J. Eng. Tribol. 226 (6) (2012) 501–515.

[41] P. Tang, Z. Zhao, H. Li, Transient temperature field short-term prediction of electric drive gearbox based on thermal network static and dynamic graph construction, Appl. Therm. Eng. 248 (2024) 123323.

[42] A. Acquaviva, A. Rodionov, A. Kersten, T. Thiringer, Y. Liu, Analytical conduction loss calculation of a mosfet three-phase inverter accounting for the reverse conduction and the blanking time, IEEE Trans. Ind. Electron. 68 (8) (2020) 6682–6691.

[43] Y. Xu, A. Kersten, S. Klacar, D. Sedarsky, Maximizing efficiency in smart adjustable dc link powertrains with igbts and sic mosfets via optimized dc-link voltage control, Batteries 9 (6) (2023) 302.

[44] T.-P. Nguyen, T.-A. Huynh, C.-W. Chang, M.-F. Hsieh, An accurate MTPA control for IPMSM considering variations of motor parameters and temperatures, in: 2023 IEEE Vehicle Power and Propulsion Conference, VPPC, IEEE, 2023, pp. 1–6.

[45] S. Li, B. Sarlioglu, S. Jurkovic, N.R. Patel, P. Savagian, Analysis of temperature effects on performance of interior permanent magnet machines for high variable temperature applications, IEEE Trans. Ind. Appl. 53 (5) (2017) 4923–4933.

[46] F. Allgöwer, A. Zheng, Nonlinear Model Predictive Control, vol. 26, Birkhäuser, 2012.

[47] C.E. Garcia, D.M. Prett, M. Morari, Model predictive control: Theory and practice—A survey, Automatica 25 (3) (1989) 335–348.

[48] J.A. Andersson, J. Gillis, G. Horn, J.B. Rawlings, M. Diehl, CasADi: a software framework for nonlinear optimization and optimal control, Math. Program. Comput. 11 (1) (2019) 1–36.

[49] J.-H. Lee, T.-G. Woo, D.-S. Jin, Y.-D. Yoon, Neural network-based MTPA control considering temperature variation in IPMSMs, in: 2024 IEEE Energy Conversion Congress and Exposition, ECCE, IEEE, 2024, pp. 6264–6269.

[50] W. Xuhui, H. Wei, F. Tao, L. Jun, Lifetime model research of motor drive system for electric vehicles, in: 2007 International Conference on Electrical Machines and Systems, ICEMS, IEEE, 2007, pp. 129–132.

[51] L. Ceccarelli, R.M. Kotecha, A.S. Bahman, F. Iannuzzo, H.A. Mantooth, Mission-profile-based lifetime prediction for a SiC MOSFET power module using a multi-step condition-mapping simulation strategy, IEEE Trans. Power Electron. 34 (10) (2019) 9698–9708.

[52] L.R. GopiReddy, L.M. Tolbert, B. Ozpineci, J.O. Pinto, Rainflow algorithm-based lifetime estimation of power semiconductors in utility applications, IEEE Trans. Ind. Appl. 51 (4) (2015) 3368–3375.

[53] S. Amirpour, T. Thiringer, D. Hagstedt, Mission-profile-based lifetime study for SiC/IGBT modules in a propulsion inverter, in: 2021 IEEE 19th International Power Electronics and Motion Control Conference, PEMC, IEEE, 2021, pp. 264–271.

[54] A. Anurag, Y. Yang, F. Blaabjerg, Thermal performance and reliability analysis of single-phase pv inverters with reactive power injection outside feed-in operating hours, IEEE J. Emerg. Sel. Top. Power Electron. 3 (4) (2015) 870–880.

[55] A. Vaccaro, P. Magnone, Influence of power cycling test methodology on the applicability of the linear damage accumulation rule for the lifetime estimation in power devices, IEEE Trans. Power Electron. 38 (5) (2023) 6545–6554.

[56] K. Tshiloz, A. Smith, A. Mohammed, S. Djurović, T. Feehally, Real-time insulation lifetime monitoring for motor windings, in: 2016 XXII International Conference on Electrical Machines, ICEM, IEEE, 2016, pp. 2335–2340.

[57] X. Zhou, Y. Ji, P. Giangrande, W. Zhao, S. Ijaz, M. Galea, Extra life loss of low voltage electrical machine under variable temperature aging, IEEE Trans. Transp. Electrification (2024).

[58] Consumer Reports, EVs offer big savings over traditional gas-powered cars, 2020, https://www.consumerreports.org/hybrids-evs/. (Accessed June 2025).

[59] L. Canals Casals, M. Rodríguez, C. Corchero, R.E. Carrillo, Evaluation of the end-of-life of electric vehicle batteries according to the state-of-health, World Electr. Veh. J. 10 (4) (2019) 63, http://dx.doi.org/10.3390/wevj10040063.